JOURNAL OF GUIDANCE, CONTROL, AND DYNAMICS
Vol. 21, No. 6, November–December 1998

# Design and Evaluation of a Three-Dimensional Optimal Ascent Guidance Algorithm

Anthony J. Calise,* Nahum Melamed,† and Seungjae Lee‡
*Georgia Institute of Technology, Atlanta, Georgia 30332*

**The problem of optimal three-dimensional guidance of a launch vehicle through the atmosphere, while satisfying a set of operational constraints and satisfying a set of tangency conditions at main engine cutoff, is considered. A hybrid analytic/numerical approach is applied to the solution of this problem. The resulting guidance algorithm makes maximum utilization of the analytically tractable portions of the solution to construct a set of interpolating functions. These functions are then used in a numerical treatment of the total problem based on the method of collocation. A numerical study is performed using a single-stage vehicle model. The results indicate that the guidance algorithm converges reliably and accurately and that the execution time required for a single guidance update is well within the realm of real-time implementation.**

## Nomenclature

$A$ = aerodynamic force in the axial direction
$A_e$ = nozzle exit area (total of active engines)
$\bar{a}$ = axial acceleration limit
$a_s$ = speed of sound
$C_A$ = axial force coefficient
$C_N$ = normal force coefficient
$c$ = nozzle exit velocity
$c_e$ = effective exit velocity
$c_1$ = Space Shuttle main engine (SSME) exit velocity
$c_2$ = RL10 exit velocity
$G$ = gravity
$g$ = $\mu/r_e^2$
$H_x$ = $\mathrm{d}\mathbf{1}_x/\mathrm{d}\boldsymbol{x} = (I_3 - \mathbf{1}_x\mathbf{1}_x^T)/|\boldsymbol{x}|$
$h$ = altitude above $r_e$, $(r - r_e)$
$M$ = Mach number
$m$ = vehicle mass
$N$ = aerodynamic force in the normal direction
$\boldsymbol{P}$ = velocity costate (primer) vector
$p_a$ = atmospheric pressure
$\boldsymbol{Q}$ = position costate vector
$q$ = dynamic pressure
$\boldsymbol{R}$ = radius vector from Earth center
$r$ = radial distance from Earth center (2-norm of $\boldsymbol{R}$)
$r_e$ = Earth radius
$S$ = reference area
$T$ = thrust
$T_{\mathrm{vac}}$ = total vacuum thrust
$T_1$ = SSME vacuum thrust (maximum thrust is equal to $\bar{T}_1$)
$T_2$ = total RL10 vacuum thrust (total maximum thrust is equal to $\bar{T}_2$)
$\boldsymbol{V}$ = inertial velocity vector
$\boldsymbol{V}_r$ = velocity relative to the air mass
$\boldsymbol{V}_w$ = wind velocity vector
$\mu$ = gravitational constant
$\rho$ = air density
$\boldsymbol{\omega}_e$ = Earth angular rate vector
$\mathbf{1}_b$ = unit vector along the body axis
$\mathbf{1}_f$ = unit vector normal to the plane containing $\boldsymbol{V}_f$ and $\boldsymbol{R}_f$
$\mathbf{1}_n$ = unit vector along $N$
$\mathbf{1}_r$ = unit vector along $R$
$\mathbf{1}_x$ = unit vector along $x$

*Subscripts*

co = RL10 cutoff
$f$ = final value
fs = specified final value
0 = initial value

## I. Introduction

TRADITIONAL launch vehicle guidance has employed open-loop guidance in the atmospheric phase and closed-loop guidance once the vehicle is sufficiently outside the atmosphere. The primary reason is that exoatmospheric formulations of the guidance problem typically have analytic or near-analytic solutions.[1,2] Though the guidance approaches for the exoatmospheric phase are efficient and reliable, the use of open-loop guidance for the atmospheric flight phase has been one cause of costly launch delays. This occurs when the actual wind profile differs significantly from the mean profile used in computing the attitude control program. The desire to reduce or eliminate this source of launch delay, together with improving payload performance, has led to a renewed interest in developing a closed-loop guidance approach for the atmospheric flight phase. Examples of such developments for two-dimensional flight can be found in Refs. 3 and 4. This effort extends the hybrid analytic/numerical approach developed in Ref. 3 to the case of three-dimensional flight, which permits optimization of out-of-plane maneuvering. In addition, several realistic constraints have been incorporated, which demonstrates the feasibility of incorporating constraints in the general procedure for guidance law development. The extension to three dimensions incorporates many of the analytical results from Refs. 5 and 6, which treat the exoatmospheric case. The algorithm can easily be modified to treat a variety of problem formulations (both atmospheric and exoatmospheric) and is not restricted to launch vehicle applications.

Section II of this paper develops the analysis that forms the basis for the hybrid guidance (HG) algorithm development. Section III describes the aerodynamic modeling used. Section IV presents simulation results. These results make use of a model for the McDonnell Douglas X-33 reusable launch vehicle (RLV). This configuration consists of a single-stage vehicle, whose propulsion system is made up of a Space Shuttle main engine (SSME) together with a cluster of RL10 propulsion units. Section V summarizes the paper.

Received Jan. 30, 1997; revision received June 12, 1998; accepted for publication June 15, 1998. 

*Professor, School of Aerospace Engineering. E-mail: anthony.calise@ae.gatech.edu. Fellow AIAA.

†Research Engineer, School of Aerospace Engineering; currently Senior Engineer, Analysis Department, Lear Astronics, 3400 Airport Avenue, Santa Monica, CA 90405. E-mail: melamed@keyway.net.

‡Graduate Research Assistant, School of Aerospace Engineering. E-mail: gt0217b@prism.gatech.edu. Student Member AIAA.

## II. Analytical Development

### A. Problem Formulation

The equations of motion for flight in a central gravitational field are expressed in an inertial, Earth-centered frame as

$$\dot{\boldsymbol{V}} = G(r)\mathbf{1}_r + \frac{(T-A)\mathbf{1}_b}{m} + \frac{N\mathbf{1}_n}{m}$$
$$\dot{\boldsymbol{R}} = \boldsymbol{V}, \qquad \dot{m} = -\frac{T_{\text{vac}}}{c} \tag{1}$$

where $T = T_{\text{vac}} - A_e p_a(r)$. The first of Eqs. (1) models thrust as aligned with the vehicle's $x$-body axis. In addition, the approximation that $G$ varies linearly with $r$ is introduced to allow analytic treatment of a portion of the dynamics[5]

$$G(r)\mathbf{1}_r = -\omega^2 \boldsymbol{R}, \qquad \omega = \sqrt{\mu/r_e^3} \tag{2}$$

For the X-33/RLV configuration, it is necessary to distinguish between thrust of the SSME and total thrust of the RL10s. Therefore, Eqs. (1) is written in the following form:

$$\dot{\boldsymbol{V}} = -\omega^2 \boldsymbol{R} + \frac{(T_1+T_2)\mathbf{1}_b}{m} + \boldsymbol{p}_V(t)$$
$$\dot{\boldsymbol{R}} = \boldsymbol{V}, \qquad \dot{m} = -\frac{T_1}{c_1} - \frac{T_2}{c_2} \tag{3}$$

where

$$\boldsymbol{p}_V(t) = \frac{-[A + A_e p_a(r)]\mathbf{1}_b + N\mathbf{1}_n}{m} + \omega^2\left(1 - \frac{1}{r^3}\right)\boldsymbol{R} \tag{4}$$

where the last term is used to compensate for the linear gravity model in Eq. (2). Note that a more complex model for gravity can be substituted for the central gravitational field model in Eq. (4). It is assumed that the initial state is specified. The objective of the HG algorithm is to control the vehicle to a set of specified end conditions during the thrusting phase of flight. The control variables are thrust level and body attitude as defined by $\mathbf{1}_b$. The index of performance is defined as the norm of the velocity vector evaluated at the final time

$$J = \|\boldsymbol{V}_f\| \tag{5}$$

In this formulation, the final mass is specified, and so maximizing the performance index in Eq. (5) is equivalent to maximizing the kinetic energy at the end of ascent. When the final altitude is also specified (as it is in this study), then it is also equivalent to maximizing the final total energy (kinetic plus potential).

Equation set (3) can be nondimensionalized using the following redefinitions for the variables:

$$\boldsymbol{R} = \boldsymbol{R}/\bar{r}, \qquad \boldsymbol{V} = \boldsymbol{V}/\bar{v}, \qquad m = m/\bar{m}$$
$$T_i = T_i/\bar{W}, \qquad A = A/\bar{W}, \qquad N = N/\bar{W} \tag{6}$$
$$c_i = c_i/\bar{v}, \qquad t = t/\bar{t}$$

where

$$\bar{r} = r_e, \qquad \bar{v} = \sqrt{\bar{r}g}, \qquad \bar{m} = m(0)$$
$$g = \mu/r_e^2, \qquad \bar{W} = \bar{m}g, \qquad \bar{t} = \bar{r}/\bar{v} \tag{7}$$

In Eq. (7), $\bar{v}$ is the circular speed at $r = r_e$. If the redefinitions in Eq. (6) are used, then Eq. (3) remains the same, except that $\omega = 1.0$ in the nondimensional version. This redefinition is applied throughout the remainder of the paper, except that all numerical results are presented in dimension form.

The thrust limits enforced are

$$T_1 \le \bar{T}_1 \tag{8}$$

$$\left.\begin{aligned} T_2 &\le \bar{T}_2 \\ T_2 &= 0 \end{aligned}\right\} \quad \begin{aligned} &\text{if} \quad h < \bar{h}_{\text{RL10}} \\ &\text{if} \quad h \ge \bar{h}_{\text{RL10}} \end{aligned} \tag{9}$$

$$(T-A)/m \le \bar{a} \tag{10}$$

The second constraint in Eq. (9) is called the RL10 cutoff condition, where $\bar{h}_{\text{RL10}}$ is the altitude above which the RL10s must be shut down. The constraint in Eq. (10) is used to limit the axial acceleration.

The final mass, radius, and flight-path angle are specified. In addition, both $\boldsymbol{R}_f$ and $\boldsymbol{V}_f$ are constrained to lie in a plane defined by a unit normal $\mathbf{1}_f$. Thus, the terminal constraints consist of

$$m_f - m_{\text{fs}} = 0 \tag{11}$$

together with the following vector of constraint expressions:

$$\psi = \begin{bmatrix} \dfrac{\boldsymbol{R}_f^T\boldsymbol{R}_f - r_{\text{fs}}^2}{2} \\ \boldsymbol{R}_f^T\mathbf{1}_f \\ \boldsymbol{V}_f^T\mathbf{1}_f \\ \boldsymbol{V}_f^T\boldsymbol{R}_f \end{bmatrix} = \mathbf{0}_4 \tag{12}$$

where $r_{\text{fs}}$ denotes the specified final radius. The last constraint in Eq. (12) has been specialized for the case of zero flight-path angle at the final time. The trajectory optimization problem from launch to main engine cutoff (MECO) is shown in Fig. 1.

### B. Optimality Conditions

The optimality conditions are obtained using the standard set of necessary conditions in optimal control.[2] The Hamiltonian for the system in Eq. (3) is given by

$$H = H_0 + H_{\text{atmos}} + \text{constraints} \tag{13}$$

where

$$H_0 = \boldsymbol{P}^T\left[-\boldsymbol{R} + \frac{(T_1+T_2)\mathbf{1}_b}{m}\right] + \boldsymbol{Q}^T\boldsymbol{V} + \lambda_m\left[-\frac{T_1}{c_1} - \frac{T_2}{c_2}\right] \tag{14}$$

$$H_{\text{atmos}} = \boldsymbol{P}^T\left[\frac{\{A - A_e p_a(r)\}\mathbf{1}_b + N\mathbf{1}_n}{m}\right]$$
$$= \boldsymbol{P}^T\boldsymbol{p}_V(t) \tag{15}$$

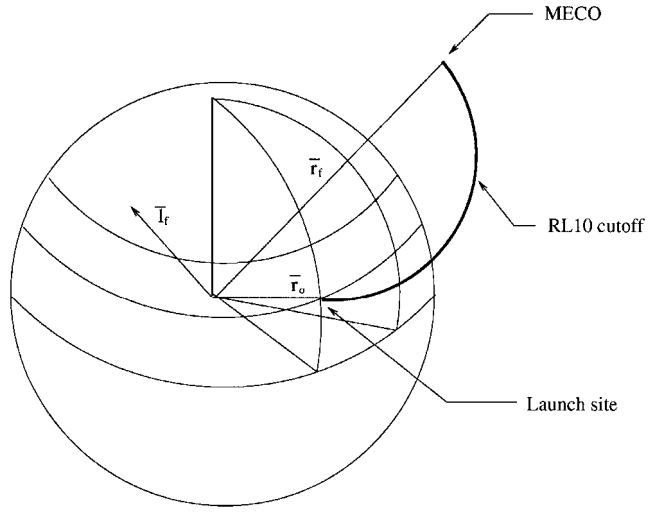


**Fig. 1 Typical ascent profile.**

and constraints in Eq. (13) consists of the constraints in Eqs. (8–10) adjoined with appropriate Lagrange multipliers. For the performance index in Eq. (5) it is assumed that the use of maximum available thrust (subject to constraints) is optimal at all times. Therefore, the control optimality condition reduces to

$$\frac{\partial H}{\partial \mathbf{1}_b} = 0 \tag{16}$$

or that $\mathbf{1}_b$ maximizes $H$. The vacuum solution ($H = H_0$) reduces to

$$\mathbf{1}_b = \mathbf{1}_p \tag{17}$$

where $\mathbf{1}_p$ is the unit vector along $\boldsymbol{P}$ (the primer vector). This result is well known in the classical literature on spacecraft trajectory optimization. The differential equations for the costate variables are

$$\dot{\boldsymbol{P}} = -\frac{\partial H}{\partial \boldsymbol{V}}, \qquad \dot{\boldsymbol{Q}} = -\frac{\partial H}{\partial \boldsymbol{R}}, \qquad \dot{\lambda}_m = -\frac{\partial H}{\partial m} \tag{18}$$

The first two expressions in Eq. (18) can be written in the following form:

$$\dot{\boldsymbol{P}} = -\boldsymbol{Q} + \boldsymbol{q}_V(t), \qquad \dot{\boldsymbol{Q}} = \boldsymbol{P} - \boldsymbol{q}_R(t) \tag{19}$$

where

$$\boldsymbol{q}_V(t) = -\frac{\partial H_{\text{atmos}}}{\partial \boldsymbol{V}}, \qquad \boldsymbol{q}_R(t) = \frac{\partial H_{\text{atmos}}}{\partial \boldsymbol{R}} \tag{20}$$

The transversality conditions for the costate variables consist of

$$\boldsymbol{P}_f = \left(\frac{\partial \psi}{\partial \boldsymbol{V}}\right)^T_{t_f} \nu + \mathbf{1}_{V_f}, \qquad \boldsymbol{Q}_f = \left(\frac{\partial \psi}{\partial \boldsymbol{R}}\right)^T_{t_f} \nu \tag{21}$$

It can easily be verified that the conditions in Eq. (21) are equivalent to the following two scalar conditions involving the final states and costates:

$$\boldsymbol{P}_f^T \boldsymbol{R}_f - \left(\frac{r_{\text{fs}}}{\|\boldsymbol{V}_f\|}\right)^2 \boldsymbol{Q}_f^T \boldsymbol{V}_f = 0, \qquad \boldsymbol{P}_f^T \mathbf{1}_{V_f} - 1 = 0 \tag{22}$$

Thus Eqs. (12) and (22) form a set of six equations that can be used to determine the six unknown initial values for the costates $\boldsymbol{P}_0$ and $\boldsymbol{Q}_0$. In the solution process, it is not necessary to solve for $\lambda_m(t)$ in constructing the control solution. Thus, it is regarded as an ignorable variable.

Because of the discontinuous nature of the RL10 constraint in Eq. (9), there is a jump that occurs in the $\boldsymbol{Q}$ costate vector at the RL10 cutoff altitude. This condition is derived from the cutoff event condition $h - \bar{h}_{\text{RL10}} = 0$. It can be shown that the jump condition reduces to

$$\boldsymbol{Q}\left(t_{\text{co}}^-\right) = \boldsymbol{Q}\left(t_{\text{co}}^+\right) - \pi \mathbf{1}_R \tag{23}$$

where

$$\pi = \left.\frac{T_2 \boldsymbol{P}^T \mathbf{1}_b}{m \mathbf{1}_R^T \boldsymbol{V}}\right|_{t = t_{\text{co}}} \tag{24}$$

The expression for the multiplier $\pi$ follows from the condition

$$H^-\left(t_{\text{co}}^-\right) = H^+\left(t_{\text{co}}^+\right) \tag{25}$$

where $H^-$ is the Hamiltonian evaluated for $T_{\text{vac}} = T_1 + T_2$ and $H^+$ is the Hamiltonian evaluated for $T_{\text{vac}} = T_1$. The continuity condition in Eq. (25) results because the cutoff event condition is not an explicit function of time.

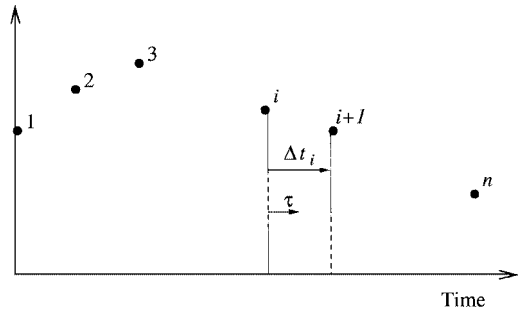


**Fig. 2 Segmented time intervals.**

### C. Vacuum Solution

The vacuum solution is constructed by solving the two-point boundary value problem associated with Eqs. (3), (19), and (23), with $\boldsymbol{p}_V(t) = \boldsymbol{q}_V(t) = \boldsymbol{q}_R(t) = 0$. At the initial time we are given $\boldsymbol{V}_0$, $\boldsymbol{R}_0$, and $m_0$. At the final time, the constraints are those given by Eqs. (12) and (22). Thrust is evaluated by using maximum vacuum thrust subject to the constraints in Eqs. (8–10), and the body attitude vector $\mathbf{1}_b$ is evaluated from the optimality condition in Eq. (17). The unknowns are the elements of the initial costate vectors $\boldsymbol{P}_0$ and $\boldsymbol{Q}_0$. The solution is constructed by developing a nearly algebraic relationship for the dependence of the terminal constraints on the unknowns and using a Newton method to numerically obtain the solution for $\boldsymbol{P}_0$ and $\boldsymbol{Q}_0$. This requires developing algebraic expressions for the solution of Eqs. (3) and (19).

In Ref. 5 it is shown, for the gravity model in Eq. (2), that the vacuum solution can be written in closed form, with the exception for the thrust terms that must be constructed by numerical quadrature. Define

$$\boldsymbol{S}(t) = \begin{bmatrix} \boldsymbol{R}(t) \\ \boldsymbol{V}(t) \end{bmatrix}, \qquad \boldsymbol{\lambda}(t) = \begin{bmatrix} \boldsymbol{P}(t) \\ -\boldsymbol{Q}(t) \end{bmatrix} \tag{26}$$

Then with reference to Fig. 2, the equations that propagate the state and costate solutions (in nondimensional form, $\omega = 1$) from time $t_i$ to $t_i + \tau$ when off the $\bar{a}$ limit are given by

$$\boldsymbol{S}(t_i + \tau) = \phi \boldsymbol{S}(t_i) + \Gamma_I \begin{bmatrix} \boldsymbol{I}_c(\tau) \\ \boldsymbol{I}_s(\tau) \end{bmatrix} \tag{27}$$

$$\boldsymbol{\lambda}(t_i + \tau) = \phi \boldsymbol{\lambda}(t_i) \tag{28}$$

$$m(t_i + \tau) = m(t_i) - (T_{\text{vac}}/c_e)\tau \tag{29}$$

where

$$\phi = \begin{bmatrix} \cos(\tau) I_3 & \sin(\tau) I_3 \\ -\sin(\tau) I_3 & \cos(\tau) I_3 \end{bmatrix}$$

$$\Gamma_I = T_{\text{vac}} \begin{bmatrix} \sin(\tau) I_3 & -\cos(\tau) I_3 \\ \cos(\tau) I_3 & \sin(\tau) I_3 \end{bmatrix} \tag{30}$$

$$c_e = \frac{c_1 c_2 (T_1 + T_2)}{c_2 T_1 + c_1 T_2} \tag{31}$$

and $I_3$ denotes a $3 \times 3$ unit matrix. In Eq. (27), $\boldsymbol{I}_c(\tau)$ and $\boldsymbol{I}_s(\tau)$ are called the thrust integrals, which are given by

$$\boldsymbol{I}_c(\tau) = \int_0^\tau \frac{\mathbf{1}_p(t_i + \sigma)\cos(\sigma)}{m(t_i + \sigma)}\, \mathrm{d}\sigma$$

$$\boldsymbol{I}_s(\tau) = \int_0^\tau \frac{\mathbf{1}_p(t_i + \sigma)\sin(\sigma)}{m(t_i + \sigma)}\, \mathrm{d}\sigma \tag{32}$$

Each thrust integral can be approximated using Simpson's rule

$$\boldsymbol{I}_x(\tau) = \frac{[\dot{\boldsymbol{I}}_x(0) + 4\dot{\boldsymbol{I}}_x(\tau/2) + \dot{\boldsymbol{I}}_x(\tau)]\tau}{6}, \qquad x = c, s \tag{33}$$

where $\dot{\boldsymbol{I}}_x(\tau)$ denotes the integrand in Eq. (32) evaluated for $\sigma = \tau$.

On the $\bar{a}$ limit, $T_{\text{vac}}/m = \bar{a}$. Consequently, $T_{\text{vac}}$ in Eq. (30) is replaced with $\bar{a}$, and $m(t)$ is deleted from the integrands of Eq. (32). Moreover, it can easily be verified that

$$m(t_i + \tau) = m(t_i)\exp[-(\bar{a}\tau/c_e)] \tag{34}$$

Equations (27–34) permit the position and velocity state and costate equations to be propagated from the initial time to any arbitrary time over the time interval of interest. In particular, a nominal solution can be generated starting from $S_0$ and $m_0$ and an initial guess for $\lambda_0$ and integrating forward until $m_f = m_{\text{fs}}$.

A Newton method with step-size regulation was used to determine $\lambda_0$ so that the terminal constraints are satisfied. The Jacobian is calculated by considering variations in the terminal constraints due to variations in $\lambda_0$, including the effect that these variations have on the jump parameter $\pi$ in Eq. (24). A variational analysis of Eqs. (27) and (28) results in a matrix difference equation, which can be swept forward to the final time and then used to numerically determine the Jacobian in an efficient manner. The details of this analysis are given in the Appendix. Thus, the Jacobian calculation is nearly analytic, except for the effect of the thrust integrals, which must be dealt with numerically.

### D. Atmospheric Solution

The atmospheric solution was constructed using a modified version of the hybrid analytic/numerical solution approach developed in Ref. 3. Numerical approaches often involve segmentation of the time interval and using simple polynomial functions to interpolate (parameterize) the solution within each segment. The coefficients of the polynomial representations are treated as additional free parameters to be determined so that both the equations of motion and the boundary conditions are approximately satisfied. The method of collocation adjusts the parameters so that continuity is preserved at the nodes, and the differential equations are satisfied at the midpoint of the intervals. The concept behind the hybrid approach of Ref. 3 is to use the easily computed (or analytically tractable) portion of a solution to develop more intelligent interpolation functions for a numerically based solution approach, such as the method of collocation. In a launch vehicle application, this amounts to using the vacuum solution to construct the interpolating function.

The hybrid solution concept is applied in its simplest form by replacing the terms $\boldsymbol{p}_V(t)$, $\boldsymbol{q}_V(t)$, and $\boldsymbol{q}_R(t)$ in Eqs. (3) and (19) with piecewise constant functions $\bar{\boldsymbol{p}}_V(t)$, $\bar{\boldsymbol{q}}_V(t)$, and $\bar{\boldsymbol{q}}_R(t)$. A second approximation employed in applying the hybrid approach to this analysis is that the vacuum optimality condition in Eq. (17) is used to eliminate the control. This approximation may be justifiable for ascent guidance on the basis that the normal component of the aerodynamic force is small compared to the axial force. In general, the approximation is not essential to the hybrid approach, and it should not be used for example in developing a guidance solution for aborts within the atmosphere. From the optimality condition below Eq. (16), the more general result is that $\mathbf{1}_b$ is aligned with the net force vector comprising the sum of the aerodynamic and propulsive forces. A correction for the difference between the vacuum solution and the actual solution can then be introduced by adding the difference, $(T_1 + T_2)(\mathbf{1}_b - \mathbf{1}_p)/m$, to Eq. (4). This approach has been validated in a later study.[7]

With the preceding simplifications, the solution to Eqs. (3) and (19) can be approximated off the $\bar{a}$ limit using

$$\boldsymbol{S}(t_i + \tau) = \phi\boldsymbol{S}(t_i) + \Gamma_I \begin{bmatrix} \boldsymbol{I}_c(\tau) \\ \boldsymbol{I}_s(\tau) \end{bmatrix} + \Gamma_p \bar{\boldsymbol{p}}_{V_i} \tag{35}$$

$$\boldsymbol{\lambda}(t_i + \tau) = \phi\boldsymbol{\lambda}(t_i) + \Gamma_q \begin{bmatrix} \bar{\boldsymbol{q}}_{V_i} \\ \bar{\boldsymbol{q}}_{R_i} \end{bmatrix} \tag{36}$$

$$m(t_i + \tau) = m(t_i) - (T_{\text{vac}}/c_e)\tau \tag{37}$$

where

$$\Gamma_p = \begin{bmatrix} (1 - \cos(\tau))I_3 \\ \sin(\tau)I_3 \end{bmatrix}$$

$$\Gamma_q = \begin{bmatrix} \sin(\tau)I_3 & (1 - \cos(\tau))I_3 \\ -(1 - \cos(\tau))I_3 & \sin(\tau)I_3 \end{bmatrix} \tag{38}$$

On the $\bar{a}$ limit, $(T - A)/m = \bar{a}$. In this case, the first of Eqs. (3) is redefined as

$$\dot{\boldsymbol{V}} = -\omega^2\boldsymbol{R} + \frac{(T - A)\mathbf{1}_b}{m} + \boldsymbol{p}_V(t) \tag{39}$$

where now $\boldsymbol{p}_V(t)$ is defined with the axial force terms in Eq. (4) deleted. As in the vacuum solution, $T_{\text{vac}}$ in Eq. (3) is replaced with $\bar{a}$ and $m(t)$ is deleted from the integrands in Eq. (32). Then, defining $\bar{A}_i$ as a piecewise constant approximation for $A(t)$ for $t_i < t < t_{i+1}$, it can easily be verified that

$$m(t_i + \tau) = (1/\bar{a})(\{m(t_i)\bar{a} + \bar{A}_i\}\exp[-(\bar{a}\tau/c_e)] - \bar{A}_i) \tag{40}$$

In the development of Ref. 3, the collocation variables are the elements of the vectors $\bar{\boldsymbol{p}}_{V_i}$, $\bar{\boldsymbol{q}}_{V_i}$, and $\bar{\boldsymbol{q}}_{R_i}$. They are treated as unknowns, together with the elements of $\boldsymbol{\lambda}_0$, and are computed using a Newton method so that both the boundary conditions are met and Eq. (20) is satisfied at the midpoints of the elements. However, implementing the approach in this manner greatly increases the dimension of the Jacobian. Moreover, the nearly analytic form developed for calculating the Jacobian for the vacuum solution would no longer apply. Thus, the approach was modified as shown in Fig. 3, which summarizes the computation procedure. The calculation starts with an initial guess for $\boldsymbol{P}_0$ and $\boldsymbol{Q}_0$ and the cut-off time $t_{\text{co}}$ and the time $t_a$ where the axial acceleration first becomes active. From this information, the final time is estimated to satisfy the final mass constraint. The first solution obtained using the Newton method corresponds to a vacuum solution in which an RL10 cutoff occurs at altitude ($\bar{h}_{\text{RL10}}$), and $t_a$ coincides with the time where the axial acceleration limit first becomes active. These times correspond to two of the nodal times indicated in Fig. 2, which are treated as adjustable nodes. The positioning of these nodes is accomplished using a simple method, based on the trajectory solution from the last iteration. For example, the adjustment of the RL10 cutoff node is calculated using

$$\delta t_{\text{co}} = \frac{\bar{h}_{\text{RL10}} - h_{\text{co}}}{\boldsymbol{V}_{\text{co}}^T\mathbf{1}_R} \tag{41}$$

where $h_{\text{co}}$, $\boldsymbol{R}_{\text{co}}$, and $\boldsymbol{V}_{\text{co}}$ are the altitude, position vector, and velocity vector at the cutoff time estimated in the previous iteration. The remaining nodes are held fixed when the loop indicated in Fig. 3 is iterated. Simultaneous with adjusting the variable nodes, the atmospheric terms are introduced in accordance with Eqs. (35–37), where the collocation parameters and $\bar{A}_i$ in Eq. (40) are computed

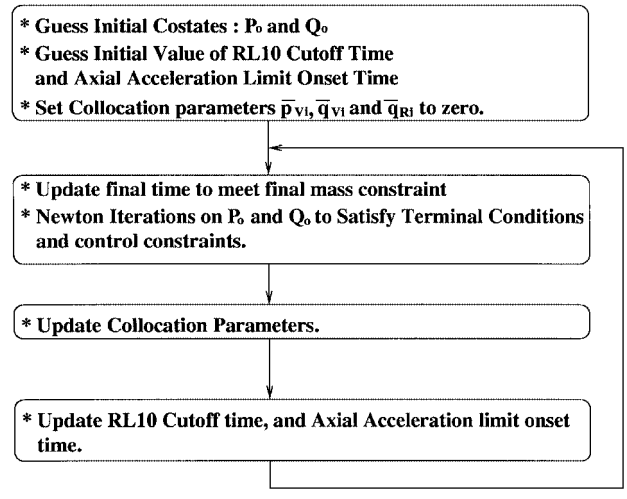


**Fig. 3 Computational procedure for incorporating atmospheric terms.**

as the average of their nodal values from the last iteration. However, rather than apply this correction to the solution process in a single step, a homotopy algorithm was employed that gradually distorts the solution from the vacuum solution to the desired final solution. The homotopy is performed by passing the computed collocation parameters through a first-order filter, so that as the process converges, the filtered outputs equal the computed values for the collocation parameters from the last iteration. An identical filter equation is used for each collocation parameter vector. For example, the filter for the elements of $\bar{\boldsymbol{p}}_{V_i}$ is given by

$$\hat{\boldsymbol{p}}_{V_i}(k) = (1-x)\hat{\boldsymbol{p}}_{V_{i-1}}(k-1) + x\bar{\boldsymbol{p}}_{V_i}(k), \qquad 0 < x < 1.0 \quad (42)$$

The filtered values are used in the next Newton iteration, which readjusts $\boldsymbol{P}_0$ and $\boldsymbol{Q}_0$ for the changes that have occurred in $t_{\text{co}}$ and $t_a$ and in the collocation variables in the outer loop. At the very start of the iteration process, $x$ is kept at zero to allow $t_{\text{co}}$ and $t_0$ to converge close to their correct values for the vacuum solution before the atmospheric effects are introduced to the solution process. Afterward, $x$ is allowed to increase linearly with the number of outer-loop iterations. This process is illustrated later when the numerical results are presented.

## III. Aerodynamic Modeling

The axial and normal aerodynamic force vectors are given by:

$$A\mathbf{1}_b = qSC_A(\alpha, M, h)\mathbf{1}_b \quad (43)$$

$$N\mathbf{1}_n = qSC_N(\alpha, M)\mathbf{1}_n \quad (44)$$

where

$$q = \frac{\rho V_r^T V_r}{2}, \qquad M = \frac{\sqrt{V_r^T V_r}}{a_s}$$
$$\mathbf{1}_n = \mathbf{1}_b \times \mathbf{1}_b \times \mathbf{1}_{V_r}, \qquad \boldsymbol{V}_r = \boldsymbol{V} - \boldsymbol{\omega}_e \times \boldsymbol{R} - \boldsymbol{V}_w \quad (45)$$

An analytical model for the aerodynamic coefficients was developed to permit the development of fully analytic expressions for the collocation parameters discussed in Sec. II. The model is defined by the following expressions:

$$C_N(\alpha, M) = C_{N_1}(M)\alpha + C_{N_2}(M)\alpha^2 + C_{N_3}(M)\alpha^3$$
$$C_A(\alpha, M, h) = C_A^{\text{inv}}(\alpha, M) + C_A^v(h, M)$$
$$C_A^{\text{inv}} = C_{A_0}^{\text{inv}}(M) + C_{A_2}^{\text{inv}}(M)\alpha^2 \quad (46)$$
$$C_A^v = C_{A_0}^v(M) + C_{A_1}^v(M)h + C_{A_2}^v(M)h^2 + C_{A_3}^v(M)h^3$$

The Mach-dependent coefficients were fitted with cubic spline polynomials.[8] The spline coefficients are computed once and stored, which permits essentially analytic determination of the force coefficients and their derivatives with respect to $h$, $M$, and $\alpha$. Spline fits were also used to represent the functional dependence of $\rho$ and $a_s$ on altitude.

## IV. Evaluation of the Guidance Algorithm

Numerical results have been generated to demonstrate the performance of the HG algorithm described in Sec. II. The initial conditions correspond to a launch at 30° latitude. The plane used to define the final conditions in Eq. (12) has an inclination of 43.7° relative to the equatorial plane, and a right ascension of essentially 0° relative to the longitude at launch. The terminal constraints require that the inertial velocity vector be turned first to the north, and later back toward the east as the vehicle approaches the final trajectory plane. The parameter values used in the calculations are $T_1 = 457{,}886.5$ lbf, $T_2 = 21{,}159 \times 6$ lbf, $c_1 = g \times 442.3$ ft/s, $c_2 = g \times 381.6$ ft/s, $S = 466$ ft$^2$, $A_{e1} = 32.64$ ft$^2$, $A_{e2} = 0.7778 \times 6$ ft$^2$, $m_0 = 280{,}000/g$ slug, $m_f = 69{,}477/g$ slug, $\mu = 1.4076E16$ ft$^3$/s$^2$, $r_e = 20{,}925{,}660$ ft, $\mathbf{1}_f = [0\ 0.5497\ -0.8353]^T$, $r_{\text{fs}} = r_e + 181{,}569$ ft, $\bar{h}_{\text{RL10}} = 90{,}000$ ft, and $\bar{a} = 4.5\ g$. The vehicle parameters correspond to a scale model intended for a demonstration phase, which was not sized to achieve orbital conditions. Consequently, the atmospheric forces are not negligible at MECO in this study. The analysis coordinate frame is an Earth-centered (up, east, north) inertial frame with the up axis passing through the launch site at the time of launch.

### A. Numerical Results

We first examine a single open-loop solution to illustrate the operation of the iteration process shown in Fig. 3. Figure 4 shows the pitch attitude as measured relative to the inertial (launch-centered) frame. Figure 4 shows how the solution is distorted from the initial vacuum solution to the final atmospheric solution, using the homotopy described for the collocation variables in Sec. II. Each solution shown represents one loop of the iteration process. The corner in the flight-path history corresponds to the RL10 cutoff time. The final converged solution starts with a pitch attitude of approximately 82 deg. The curvature in pitch attitude before and after RL10 cutoff is indicative of the nonoptimality of linear tangent steering (Ref. 2) within the atmosphere. These results were generated for zero wind conditions. A total of 33 nodes were used so that the results are very accurate, and the plots have a smooth appearance. However, experience with the algorithm has shown that 10–12 nodes still provide a high degree of accuracy in the guidance solution, as will be shown shortly.

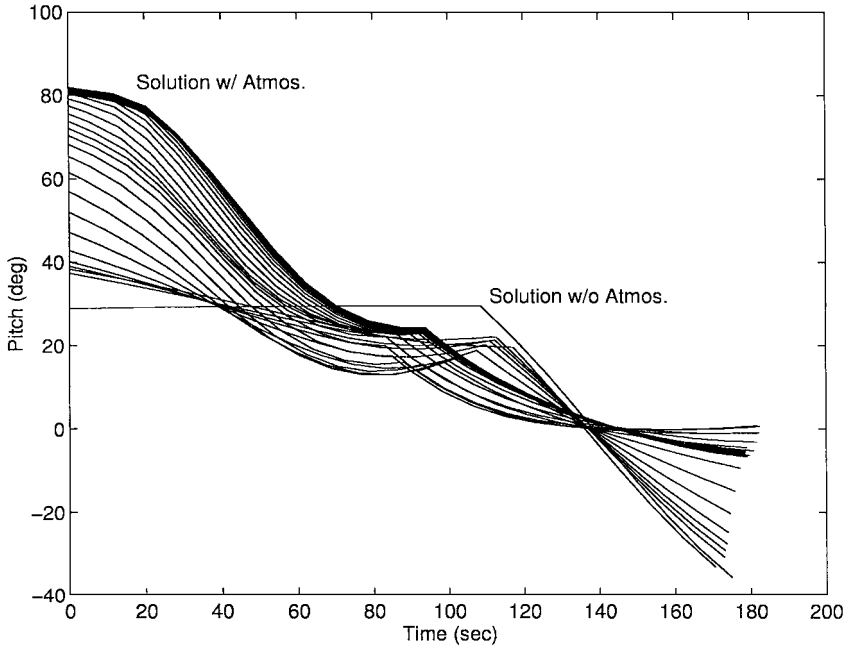


**Fig. 4 Evolution of the pitch attitude response.**

The results of six cases are summarized in Tables 1 and 2. Table 1 summarizes the open-loop results. The open-loop results correspond to applying the control time history computed at launch for the no wind case (case 1) and recording the terminal errors at burn-out, together with the final velocity at burn-out. The control solution (three-dimensional attitude command) is updated by propagation of the open-loop primer vector solution in 1.0-s intervals. The case 1 terminal errors in Table 1 represent the predictive capabilities of the guidance solution from the time of launch, which is quite good considering that only 10 evenly spaced fixed nodes were used in calculating the hybrid solution. The horizontal wind profiles used in the case 2 results correspond to the mean wind profile for the Kennedy Space Center (KSC). Case 3 used a wind shear profile invented for this study. These profiles are the same as those used in the two-dimensional study of Ref. 3. Cases 4–6 examine the effect of an off-nominal thrust (0.965 nominal) without and with the effects of the wind profiles. Note that the terminal errors are significantly higher in cases 4–6 than in cases 2 and 3. This indicates that terminal errors are significantly more sensitive to thrust dispersions than they are to wind dispersions.

**Table 1 Terminal errors for the open-loop case**

| Errors | Altitude, ft | Lat. pos., ft | Lat. vel., ft | $\Gamma$, deg | $V_f$, ft/s |
|---|---|---|---|---|---|
| Case 1[a] | −1.3229*E*3 | −2.5533*E*2 | 6.8098 | 0.1119 | 1.4363*E*4 |
| Case 2[b] | −2.8481*E*3 | 4.1233*E*3 | 1.8871 | 0.0565 | 1.4308*E*4 |
| Case 3[c] | −1.8051*E*3 | −5.3075*E*3 | −2.5557*E*1 | 0.1193 | 1.4375*E*4 |
| Case 4[d] | −2.5369*E*4 | −2.5065*E*4 | −4.4062*E*2 | −0.9170 | 1.3577*E*4 |
| Case 5[e] | −2.6823*E*4 | −2.0889*E*4 | −4.6436*E*2 | −0.9940 | 1.3530*E*4 |
| Case 6[f] | −2.6201*E*4 | −3.0220*E*4 | −4.7976*E*2 | −0.9337 | 1.3578*E*4 |

[a]Open-loop guidance, no wind.
[b]Open-loop guidance with KSC wind.
[c]Open-loop guidance with windshear.
[d]Open-loop guidance with 0.965 thrust, no wind.
[e]Open-loop guidance with 0.965 thrust with KSC wind.
[f]Open-loop guidance with 0.965 thrust with windshear.

**Table 2 Terminal errors for the closed-loop case**

| Errors | Altitude, ft | Lat. pos., ft | Lat. vel., ft | $\Gamma$, deg | $V_f$, ft/s |
|---|---|---|---|---|---|
| Case 1 | −1.8440 | 5.2736 | −1.1063 | −2.2437*E*-3 | 1.4381*E*4 |
| Case 2 | −1.7165 | 4.9763 | −0.3983 | −2.8029*E*-4 | 1.4372*E*4 |
| Case 3 | −2.9725 | 6.0564 | −2.9980 | −9.0229*E*-3 | 1.4387*E*4 |
| Case 4 | −0.6390 | 2.3730 | −2.9800 | −6.1779*E*-3 | 1.3770*E*4 |
| Case 5 | −0.3958 | −2.3234 | −1.7957 | −2.5584*E*-3 | 1.3761*E*4 |
| Case 6 | −0.4049 | 1.9700 | −1.1879 | 1.3638*E*-4 | 1.3753*E*4 |

The closed-loop guidance solution was obtained by recalculating the open-loop solution in 10.0-s intervals during the flight and updating the control solution in open-loop fashion in 1.0-s intervals between guidance updates. Table 2 summarizes the closed-loop results. Note that the terminal errors are essentially zero in all of these cases and that the improvements in terminal velocity are much less dramatic. For example, the speed gained from closed-loop guidance is approximately 30 ft/s in case 5. Therefore, the main benefit of closed-loop guidance is to reduce terminal errors, and the improvement (over open-loop guidance) in terminal velocity is secondary. However, it should be noted that we are measuring dispersions relative to an optimal open-loop solution. Comparisons of terminal velocity to another (nonoptimal) guidance scheme may be more dramatic.

The open- and closed-loop altitude and axial acceleration profiles for case 6 are compared in Figs. 5 and 6 (guided solution shown by dotted line). The RL10 cutoff and axial acceleration limit times are plainly visible in Fig. 6. It was observed that the wind shear profile used in case 6 resulted in peaks in the normal acceleration profile (see Ref. 8). These peaks can be significantly reduced by using day-of-launch profiles in the guidance solution, so that the guidance solution is only subjected to dispersions from DOL data. In addition, standard load alleviation methods can be used in the flight control loop to limit normal acceleration. Figure 7 shows how the components of the primer vector (used to calculate the attitude command) propagate with and without guidance updates. The effect of the guidance updates can be seen as small jumps in the solid lines in this figure. Although the corrections that take place after 90 s of flight time are very small, the corrections near the end of the trajectory are essential to reducing terminal errors. A similar comparison of the position costate elements is shown in Fig. 8. The jump in the up costate component due to the RL10 cutoff condition is clearly visible. The north and east components are nearly constant.

Finally, Fig. 9 summarizes the operation of the outer-loop iteration process as described earlier. Figure 9 displays the computed estimates for final time (∗), RL10 cutoff time (○) and the time-of-onset for the longitudinal acceleration limit (+). The computed values at each guidance update are plotted as a function of the total number of outer-loop iterations. Approximately 42 outer-loop iterations were performed to obtain the first guidance solution (this can be performed prior to launch), and Fig. 9 shows how the iteration count progresses at each guidance update. In general, the inner loop requires 1–3 iterations for each outer-loop iteration. Once the first solution is converged, significantly fewer outer iterations are required between guidance updates. The results in Fig. 9 and in Tables 1 and 2 strongly suggest that the outer-loop iteration can

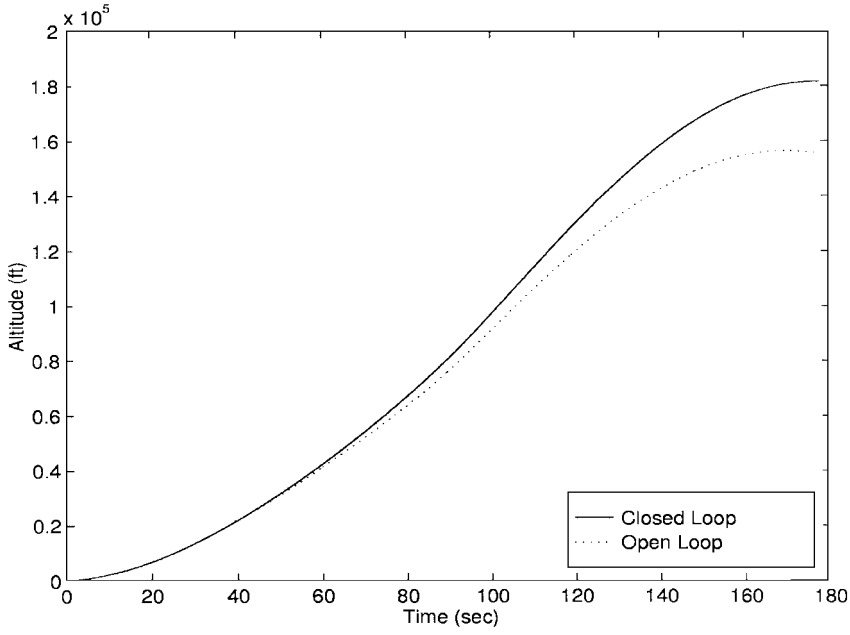


**Fig. 5 Altitudes profile for case 6.**

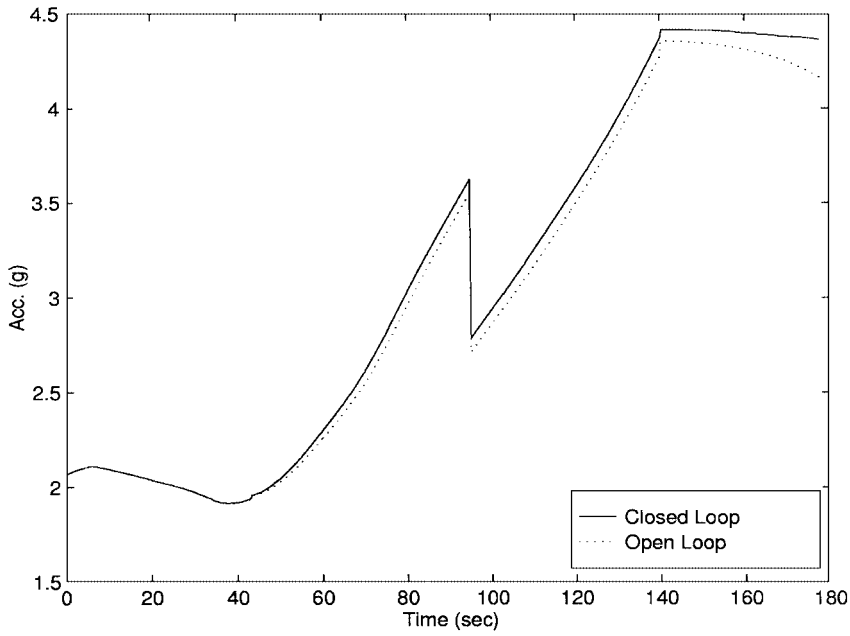


**Fig. 6 Axial acceleration for case 6.**

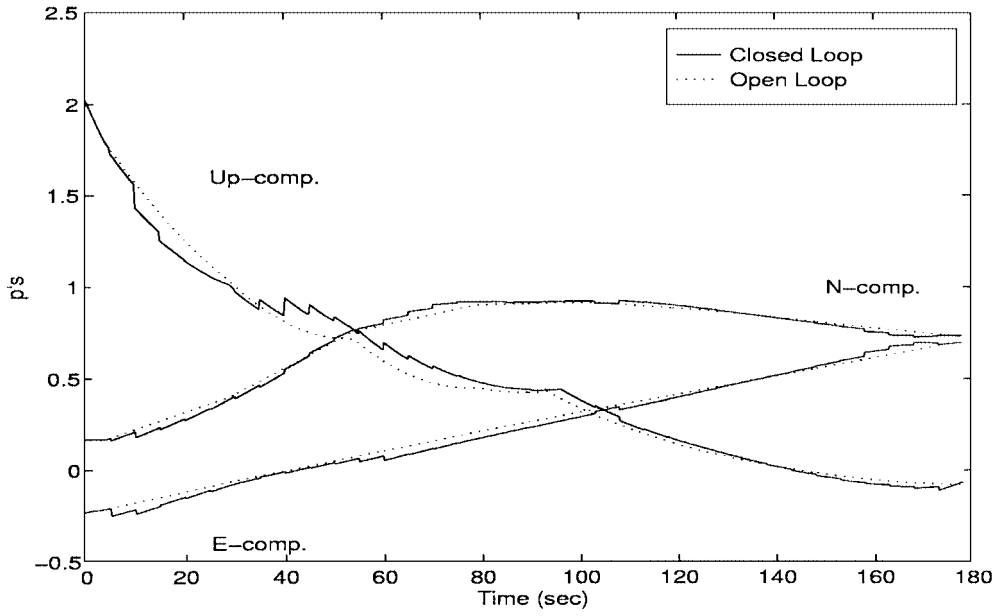


**Fig. 7 Velocity costate values along the guided path for case 6.**

easily be eliminated and that only the inner-loop iteration should be retained to maintain terminal errors close to zero. Not only are the changes in the outer-loop variables small, the guidance loop only needs an approximate representation of times when path constraints are enforced, whereas the actual enforcement of these constraints can be accomplished more accurately outside the guidance loop by using the onboard sensors.

### B. Comments on the Algorithm

The Newton method converges to machine precision, if a suitable initial guess is provided. The initial solution at launch can be computed prior to launch. This provides a highly reliable starting guess for subsequent updates of the algorithm. In general, only several iterations are required to update the solution using a prior converged solution. At any stage during the flight, a full open-loop guidance solution from the current time to MECO is always available from the last update in the event that the Newton method fails to converge. Our current estimate is that guidance updates can be completed in less than a second of execution time using a 130-MHz processor. In addition, execution time and utilization of the guidance algorithm can be significantly enhanced (by at least a factor of 10) by using small angle approximations [e.g., Eq. (30)] and by eliminating the outer-loop iteration in Fig. 3 during flight.

The algorithm can easily be modified to handle different performance indices or different sets of terminal constraints and associated tangency conditions both at the initial time and the final time. In general, it is not limited to launch vehicle applications. Such changes should require modest modifications to the derivations of the necessary conditions and the variational analysis contained in the Appendix. Use of the vacuum optimality condition in Eq. (17) can result in serious loss of optimality for trajectories in the atmosphere involving higher angle-of-attack profiles, such as may be encountered during a abort maneuver. The procedure for removing this approximation has been suggested in Ref. 3. The full optimality condition from Eq. (16) contains atmospheric terms, which have been neglected in Eq. (17). When the full optimality condition is employed, $\mathbf{1}_b$ will contain a component normal to $\mathbf{1}_p$, which, after substitution for $\mathbf{1}_p$ in the equations of motion, results in additional

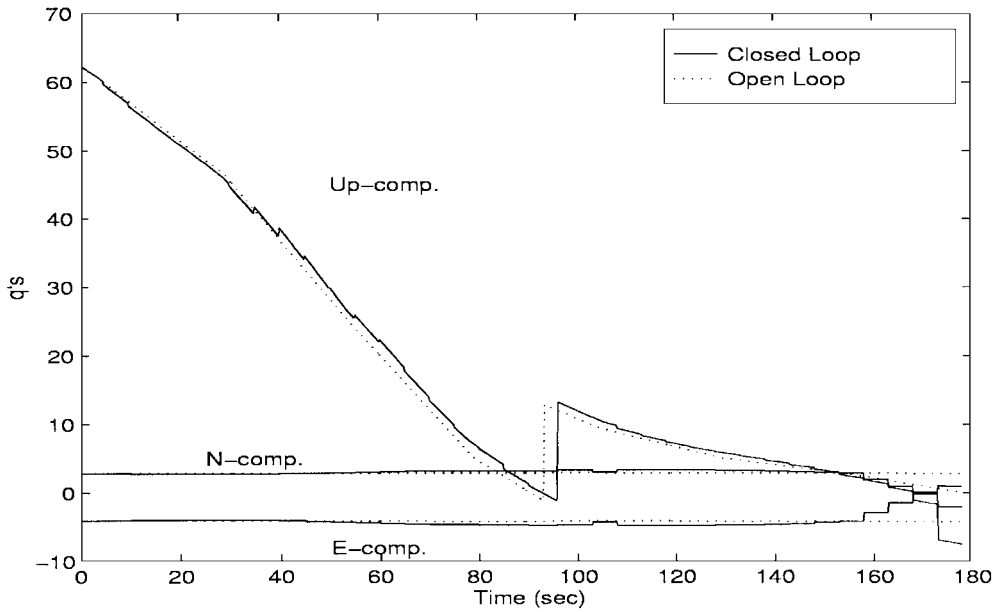


**Fig. 8 Position costate values along the guided path for case 6.**

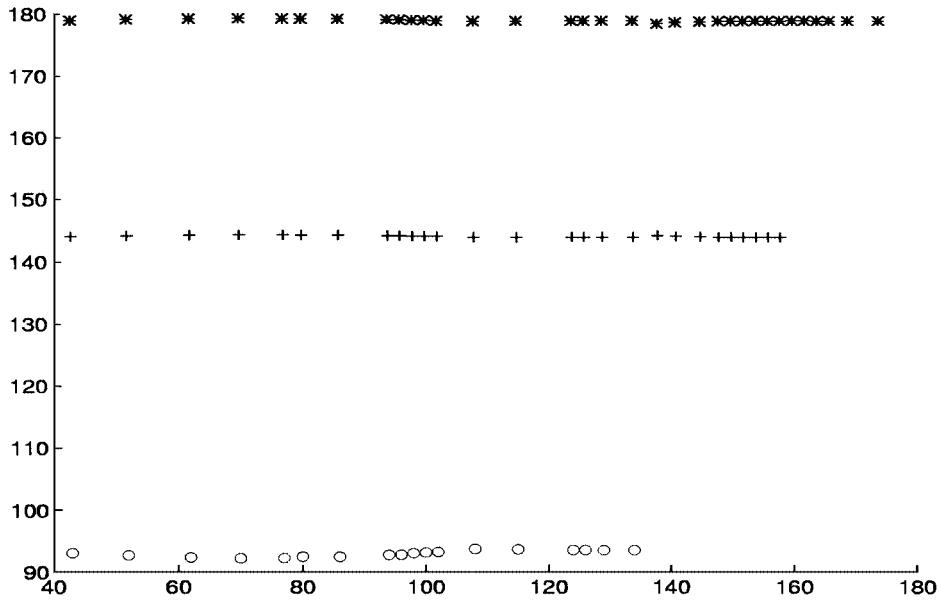

**Fig. 9 RL10 cutoff time, axial limit time, and $t_f$ vs outer-loop iteration count.**

aerodynamic terms that can then be incorporated as a part of the definition of the collection variables in Eqs. (3) and (19).[7] Path constraints, such as normal force or $\alpha$ limits, $q$ limits, and $\alpha q$ limits, may be added by noting that these introduce additional terms to the Hamiltonians, as suggested by Eq. (13). Normal force and $\alpha$ limits are enforced by limiting the solution for $\mathbf{1}_b$ and computing the associated constraint multiplier from Eq. (16). Dynamic pressure limits are enforced by limiting the throttle when this constraint is encountered. Active constraints introduce additional terms into $\boldsymbol{p}_V(t)$, $\boldsymbol{q}_R(t)$, and $\boldsymbol{q}_V(t)$, without changing the architecture of the algorithm and the Jacobian calculation. This is one of the major advantages of the computational procedure described in Fig. 3. Reference 7 contains numerical results with normal force limits and extends the problem formulation to vehicles with staging constraints, discontinuous mass changes, and boundary conditions for attaining orbits specified by apogee, perigee, and inclination.

One fundamental limitation of the approach is that the modeling assumes mass flow is a linear function of thrust. Therefore, it is recommended that energy state approximations and reduced-order modeling methods be used for vehicles with air-breathing propulsion systems, an example of which may be found in Ref. 9.

## V. Conclusions

An HG algorithm for ascent guidance of the McDonnell Douglas, X-33 RLV configuration has been developed and evaluated in a non-real-time environment. The algorithm can be used to obtain both vacuum solutions and solutions within the atmosphere. The optimization interval is from any starting condition to a terminal condition at MECO, and some operational constraints are enforced. The major conclusion from this preliminary effort is that real-time optimal guidance is feasible for the atmospheric flight phase. The Newton algorithm converges reliably to machine precision. The starting solution can be computed prior to launch and later updated in real time at intervals along the flight trajectory. Real-time updates should require only several Newton steps, and execution times should be on order of 1 s or less. Furthermore, the algorithm can be modified to treat a wide variety of problem formulations of interest in flight mechanics.

## Appendix: Variational Analysis

This Appendix outlines the steps in a variational analysis to derive the expression for the Jacobian that relates variations in the

initial costates to variations in the terminal constraints and tangency conditions at the terminal time.

**State and Costate Variation**

Define $\boldsymbol{U}^T = [\boldsymbol{S}^T \;\; \boldsymbol{\lambda}^T]$ and $\boldsymbol{J}^T = [\boldsymbol{I}_c^T(\tau) \;\; \boldsymbol{I}_s^T(\tau)]$. Then the variation of Eqs. (35) and (36) due to variations in $\boldsymbol{\lambda}_0$ can be written as

$$\mathrm{d}\boldsymbol{U}(t_i+\tau) = \Phi(\tau)\,\mathrm{d}\boldsymbol{U}(t_i), \qquad \mathrm{d}\boldsymbol{U}^T(t_0) = \begin{bmatrix} 0 & d\boldsymbol{\lambda}_0^T \end{bmatrix} \tag{A1}$$

where

$$\Phi(\tau) = \begin{bmatrix} \phi & \Gamma_I \dfrac{\mathrm{d}\boldsymbol{J}(\tau)}{\mathrm{d}\boldsymbol{\lambda}(t_i)} \\ 0 & \phi \end{bmatrix} \tag{A2}$$

and $\tau = t - t_i$, where $t_i$ are the nodal times as shown in Fig. 2. From Eq. (33) we have

$$\mathrm{d}\boldsymbol{I}_x(\tau) = \frac{[\mathrm{d}\dot{\boldsymbol{I}}_x(0) + 4\mathrm{d}\dot{\boldsymbol{I}}_x(\tau/2) + \mathrm{d}\dot{\boldsymbol{I}}_x(\tau)]\tau}{6} \tag{A3}$$

For $x = c$ and $s$,

$$\dot{\boldsymbol{I}}_c(\tau) = \frac{\boldsymbol{P}(\tau)\cos(\tau)}{m(\tau)|\boldsymbol{P}(\tau)|}, \qquad \dot{\boldsymbol{I}}_s(\tau) = \dot{\boldsymbol{I}}_c(\tau)\tan(\tau) \tag{A4}$$

and, therefore,

$$\mathrm{d}\dot{\boldsymbol{I}}_c(\tau) = \frac{\cos(\tau)}{m(\tau)|\boldsymbol{P}(\tau)|}\left[\mathrm{d}\boldsymbol{P} - \frac{(\boldsymbol{P}(\tau)^T\,\mathrm{d}\boldsymbol{P})\boldsymbol{P}(\tau)}{|\boldsymbol{P}(\tau)|^2}\right] \tag{A5}$$

where from Eq. (28) it follows that

$$\mathrm{d}\boldsymbol{P} = [\cos(\tau)I_3 \quad \sin(\tau)I_3]\,\mathrm{d}\boldsymbol{\lambda}(t_i) = \Lambda(\tau)\,\mathrm{d}\boldsymbol{\lambda}(t_i) \tag{A6}$$

Using Eq. (A6) in Eq. (A5),

$$\begin{aligned}\mathrm{d}\dot{\boldsymbol{I}}_c(\tau) &= \frac{\cos(\tau)}{m(\tau)|\boldsymbol{P}(\tau)|}\left[I_3 - \frac{\boldsymbol{P}(\tau)\boldsymbol{P}(\tau)^T}{|\boldsymbol{P}(\tau)|^2}\right]\Lambda(\tau)\,\mathrm{d}\boldsymbol{\lambda}(t_i) \\ &= K(\tau)\,\mathrm{d}\boldsymbol{\lambda}(t_i)\end{aligned} \tag{A7}$$

and using Eq. (A7) in Eq. (A3) for $x = c$,

$$\frac{\mathrm{d}\boldsymbol{I}_c(\tau)}{\mathrm{d}\boldsymbol{\lambda}(t_i)} = \frac{[K(0) + 4K(\tau/2) + K(\tau)]\tau}{6} \tag{A8}$$

Also, from Eq. (A4)

$$\frac{\mathrm{d}\boldsymbol{I}_s(\tau)}{\mathrm{d}\boldsymbol{\lambda}(t_i)} = \frac{[4K(\tau/2)\tan(\tau/2) + K(\tau)\tan(\tau)]\tau}{6} \tag{A9}$$

Equations (A8) and (A9) are used to calculate the 1, 2 element of $\Phi(\tau)$ in Eq. (A2). Equation (A1) is used with $\tau = (t_{i+1} - t_i)$ to propagate the variation from one node in Fig. 2 to the next.

**Variation of the Jump Condition**

From Eq. (23), the variation of the jump condition can be expressed as

$$\mathrm{d}\boldsymbol{U}\left(t_{\mathrm{co}}^+\right) = \left\{\boldsymbol{I}_{12} - \begin{bmatrix} 0 \\ I_3 \end{bmatrix}\frac{\mathrm{d}(\pi\mathbf{1}_R)}{\mathrm{d}U}\right\}\mathrm{d}\boldsymbol{U}\left(t_{\mathrm{co}}^-\right) = M_{\mathrm{co}}\,\mathrm{d}\boldsymbol{U}\left(t_{\mathrm{co}}^-\right) \tag{A10}$$

where it can be shown that

$$\begin{aligned}\frac{\mathrm{d}(\pi\mathbf{1}_R)}{\mathrm{d}U} &= \begin{bmatrix}\left(\mathbf{1}_R\boldsymbol{\pi}_R^T + \pi H_R\right) & \mathbf{1}_R\boldsymbol{\pi}_V^T & \mathbf{1}_R\boldsymbol{\pi}_P^T & 0\end{bmatrix} \\ H_R &= \frac{\mathrm{d}\mathbf{1}_R}{\mathrm{d}\boldsymbol{R}} = \frac{I_3 - \mathbf{1}_R\mathbf{1}_R^T}{|\boldsymbol{R}|}, \qquad \boldsymbol{\pi}_R = -k_1 H_R \boldsymbol{V}\end{aligned} \tag{A11}$$

$$\boldsymbol{\pi}_V = -k_1\mathbf{1}_R, \qquad \boldsymbol{\pi}_R = -k_1\left(\mathbf{1}_R^T\boldsymbol{V}\right)\mathbf{1}_P, \qquad k_1 = \frac{T_2|\boldsymbol{P}|}{m\left(\mathbf{1}_R^T\boldsymbol{V}\right)^2}$$

**Variation on the Acceleration Limit**

On the longitudinal acceleration limit, the thrust integrals are modified as described in text leading to Eq. (40). Thus, the definition of $\Gamma_I$ in Eq. (30) with $T_{\mathrm{vac}}$ replaced by $\bar{a}$ applies in Eq. (A2), and $m(\tau)$ is deleted Eq. (A7).

**Propagation of the Variation in Initial Costates**

Using Eq. (A1) together with the jump condition in Eq. (A10), the variation in terminal states and costates is given by

$$\mathrm{d}\boldsymbol{U}_f = \begin{bmatrix}\mathrm{d}\boldsymbol{S}_f \\ \mathrm{d}\boldsymbol{\lambda}_f\end{bmatrix} = \Phi^+ M_{\mathrm{co}}\Phi^- \begin{bmatrix} 0 \\ \mathrm{d}\boldsymbol{\lambda}_0\end{bmatrix} = \Theta\begin{bmatrix} 0 \\ \mathrm{d}\boldsymbol{\lambda}_0\end{bmatrix} \tag{A12}$$

where $\Phi^-$ and $\Phi^+$ represent the propagations from $t_0$ to $t_{\mathrm{co}}$ and from $t_{\mathrm{co}}$ to $t_f$, respectively. For example,

$$\Phi^- = \prod_{i=1}^{k}\Phi(t_{i+1} - t_i) \tag{A13}$$

where $k$ is the node corresponding to $t = t_{\mathrm{co}}$.

**Calculation of the Jacobian**

There are six boundary conditions at the final time defined by the four terminal constraints in Eq. (12) and the two transversality conditions in Eq. (22). Writing these constraints in the form

$$\Psi(\boldsymbol{S}_f, \boldsymbol{\lambda}_f) = 0 \tag{A14}$$

then, using Eq. (A12), it follows that

$$\mathrm{d}\boldsymbol{\Psi} = \Psi_S\,\mathrm{d}\boldsymbol{S}_f + \Psi_\lambda\,\mathrm{d}\boldsymbol{\lambda}_f = (\Psi_S\Theta_{1,2} + \Psi_\lambda\Theta_{2,2})\,\mathrm{d}\boldsymbol{\lambda}_0 \tag{A15}$$

where $\Theta_{i,j}$ is a $6\times 6$ subblock in the matrix $\Theta$. Hence,

$$\mathrm{Jacob} \equiv \frac{\mathrm{d}\boldsymbol{\Psi}}{\mathrm{d}\boldsymbol{\lambda}_0} = \Psi_S\Theta_{1,2} + \Psi_\lambda\Theta_{2,2} \tag{A16}$$

where

$$\begin{aligned}\Psi_S &= [\Psi_R \quad \Psi_V], \qquad \Psi_\lambda = [\Psi_P \quad -\Psi_Q] \\ \Psi_R^T &= [\boldsymbol{R} \quad \mathbf{1}_f \quad 0 \quad \boldsymbol{V} \quad \boldsymbol{P} \quad 0]_f \\ \Psi_V^T &= \left[0 \quad 0 \quad \mathbf{1}_f \quad \boldsymbol{R} \quad -k_3^2\bar{\boldsymbol{Q}} \quad H_V\boldsymbol{P}\right]_f \\ \Psi_P^T &= [0 \quad 0 \quad 0 \quad 0 \quad \boldsymbol{R} \quad \mathbf{1}_V]_f \\ \Psi_Q^T &= \left[0 \quad 0 \quad 0 \quad 0 \quad -k_3^2\boldsymbol{V} \quad 0\right]_f \\ k_3 &= \frac{\|r_{\mathrm{fs}}\|}{\|\boldsymbol{V}\|}, \qquad \bar{\boldsymbol{Q}} = \boldsymbol{Q} - 2\left(\boldsymbol{Q}^T\mathbf{1}_r\right)\mathbf{1}_r\end{aligned} \tag{A17}$$

## Acknowledgment

This research has been supported by McDonnell Douglas Company, now called Boeing Company, Space Systems.

## References

[1]Marec, J. P., *Optimal Space Trajectories*, Elsevier Scientific, New York, 1979, Chap. 6.

[2]Bryson, A. E., Jr., and Ho, Y.-C., *Applied Optimal Control*, Hemisphere, New York, 1975, Chap. 2.

[3]Leung, M. S. K., and Calise, A. J., "Hybrid Approach to Near-Optimal Launch Vehicle Guidance," *Journal of Guidance, Control, and Dynamics*, Vol. 17, No. 5, 1994, pp. 881–888.

[4]Feeley, T. S., and Speyer, J. L., "Techniques for Developing Approximate Optimal Advanced Launch System Guidance," *Journal of Guidance, Control, and Dynamics*, Vol. 17, No. 5, 1994, pp. 889–896.

[5]McAdoo, S. F., Jezewski, D. J., and Dawkins, G. S., "Development of a Method for Optimal Maneuver Analysis of Complex Space Missions," NASA TN D-7882, April 1975.

[6]Jezewski, D. J., "OMEGA—An Approximate Analytic Solution of N-Burn Optimal Trajectories," NASA Manned Spacecraft Center, Internal Note 72-FM-232, Houston, TX, Sept. 1972.

[7]Calise, A. J., "Development of an Ascent Guidance Algorithm for Launch Vehicle Synthesis," Boeing Co. Phantom Works/Advanced Space, Final Rept., Agreement CA-04-97-004H, Huntington Beach, CA, Jan. 1998.

[8]Calise, A. J., and Melamed, N., "Design and Evaluation of a Hybrid Ascent Guidance Algorithm for the X-33," McDonnell Douglas Corp., Final Rept., Contract Agreement CA-05-95-25H, June 1996.

[9]Corban, J. E., Calise, A. J., and Flandro, G. A., "Rapid Near-Optimal Aerospace Plane Trajectory Generation and Guidance," *Journal of Guidance, Control, and Dynamics*, Vol. 14, No. 6, 1991, pp. 1181–1190.